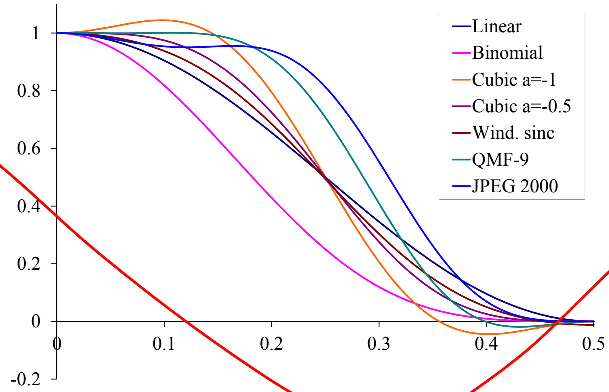


**Figure 3.31** Frequency response for some $2\times$ decimation filters. The cubic $a = -1$ filter has the sharpest fall-off but also a bit of ringing; the wavelet analysis filters (QMF-9 and JPEG 2000), while useful for compression, have more aliasing.

- a cosine-windowed sinc function (Table 3.2);
- the QMF-9 filter of Simoncelli and Adelson (1990b) is used for wavelet denoising and aliases a fair amount (note that the original filter coefficients are normalized to $\sqrt{2}$ gain so they can be "self-inverting");
- the 9/7 analysis filter from JPEG 2000 (Taubman and Marcellin 2002).

Please see the original papers for the full-precision values of some of these coefficients.

### 3.5.3 Multi-resolution representations

Now that we have described interpolation and decimation algorithms, we can build a complete image pyramid (Figure 3.32). As we mentioned before, pyramids can be used to accelerate coarse-to-fine search algorithms, to look for objects or patterns at different scales, and to perform multi-resolution blending operations. They are also widely used in computer graphics hardware and software to perform fractional-level decimation using the MIP-map, which we cover in Section 3.6.

The best known (and probably most widely used) pyramid in computer vision is Burt and Adelson's (1983a) Laplacian pyramid. To construct the pyramid, we first blur and subsample the original image by a factor of two and store this in the next level of the pyramid (Figure 3.33). Because adjacent levels in the pyramid are related by a sampling rate $r = 2$, this kind of pyramid is known as an *octave pyramid*. Burt and Adelson originally proposed a

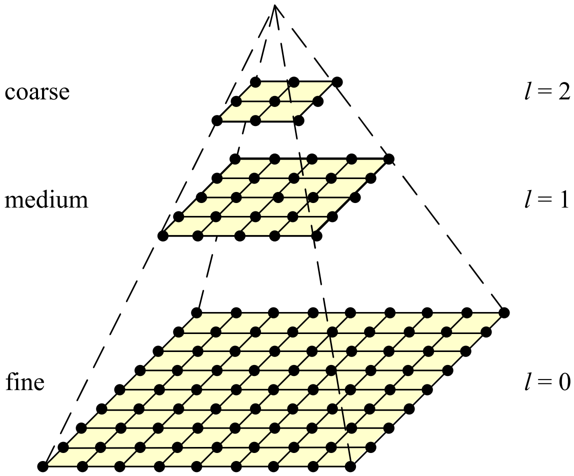


**Figure 3.32** A traditional image pyramid: each level has half the resolution (width and height), and hence a quarter of the pixels, of its parent level.

five-tap kernel of the form

$$\boxed{c \mid b \mid a \mid b \mid c}, \tag{3.82}$$

with $b = 1/4$ and $c = 1/4 - a/2$. In practice, $a = 3/8$, which results in the familiar binomial kernel,

$$\frac{1}{16}\boxed{1 \mid 4 \mid 6 \mid 4 \mid 1}, \tag{3.83}$$

which is particularly easy to implement using shifts and adds. (This was important in the days when multipliers were expensive.) The reason they call their resulting pyramid a *Gaussian* pyramid is that repeated convolutions of the binomial kernel converge to a Gaussian.[16]

To compute the *Laplacian* pyramid, Burt and Adelson first interpolate a lower resolution image to obtain a *reconstructed* low-pass version of the original image (Figure 3.34b). They then subtract this low-pass version from the original to yield the band-pass "Laplacian" image, which can be stored away for further processing. The resulting pyramid has *perfect reconstruction*, i.e., the Laplacian images plus the base-level Gaussian ($L_2$ in Figure 3.34b) are sufficient to exactly reconstruct the original image. Figure 3.33 shows the same computation in one dimension as a signal processing diagram, which completely captures the computations being performed during the analysis and re-synthesis stages.

Burt and Adelson also describe a variant on the Laplacian pyramid, where the low-pass image is taken from the original blurred image rather than the reconstructed pyramid (piping the output of the $L$ box directly to the subtraction in Figure 3.34b). This variant has less

[16] Then again, this is true for any smoothing kernel (Wells 1986).

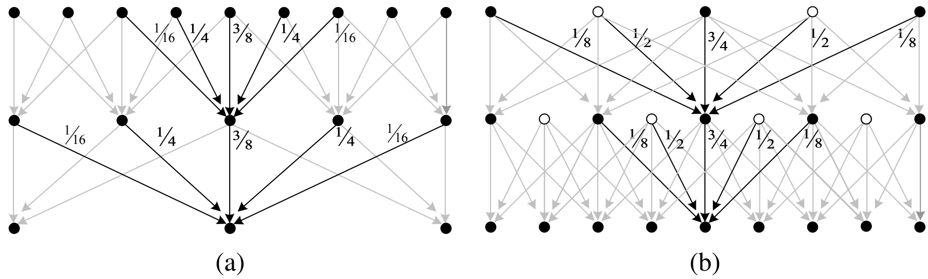


**Figure 3.33** The Gaussian pyramid shown as a signal processing diagram: The (a) analysis and (b) re-synthesis stages are shown as using similar computations. The white circles indicate zero values inserted by the $\uparrow 2$ upsampling operation. Notice how the reconstruction filter coefficients are twice the analysis coefficients. The computation is shown as flowing down the page, regardless of whether we are going from coarse to fine or *vice versa*.

aliasing, since it avoids one downsampling and upsampling round-trip, but it is not self-inverting, since the Laplacian images are no longer adequate to reproduce the original image.

As with the Gaussian pyramid, the term Laplacian is a bit of a misnomer, since their band-pass images are really differences of (approximate) Gaussians, or DoGs,

$$\mathrm{DoG}\{I; \sigma_1, \sigma_2\} = G_{\sigma_1} * I - G_{\sigma_2} * I = (G_{\sigma_1} - G_{\sigma_2}) * I. \tag{3.84}$$

A Laplacian of Gaussian (which we saw in (3.26)) is actually its second derivative,

$$\mathrm{LoG}\{I; \sigma\} = \nabla^2 (G_\sigma * I) = (\nabla^2 G_\sigma) * I, \tag{3.85}$$

where

$$\nabla^2 = \frac{\partial^2}{\partial x^2} + \frac{\partial^2}{\partial y^2} \tag{3.86}$$

is the Laplacian (operator) of a function. Figure 3.35 shows how the Differences of Gaussian and Laplacians of Gaussian look in both space and frequency.

Laplacians of Gaussian have elegant mathematical properties, which have been widely studied in the *scale-space* community (Witkin 1983; Witkin, Terzopoulos, and Kass 1986; Lindeberg 1990; Nielsen, Florack, and Deriche 1997) and can be used for a variety of applications including edge detection (Marr and Hildreth 1980; Perona and Malik 1990b), stereo matching (Witkin, Terzopoulos, and Kass 1987), and image enhancement (Nielsen, Florack, and Deriche 1997).

A less widely used variant is *half-octave pyramids*, shown in Figure 3.36a. These were first introduced to the vision community by Crowley and Stern (1984), who call them *Difference of Low-Pass* (DOLP) transforms. Because of the small scale change between adja-

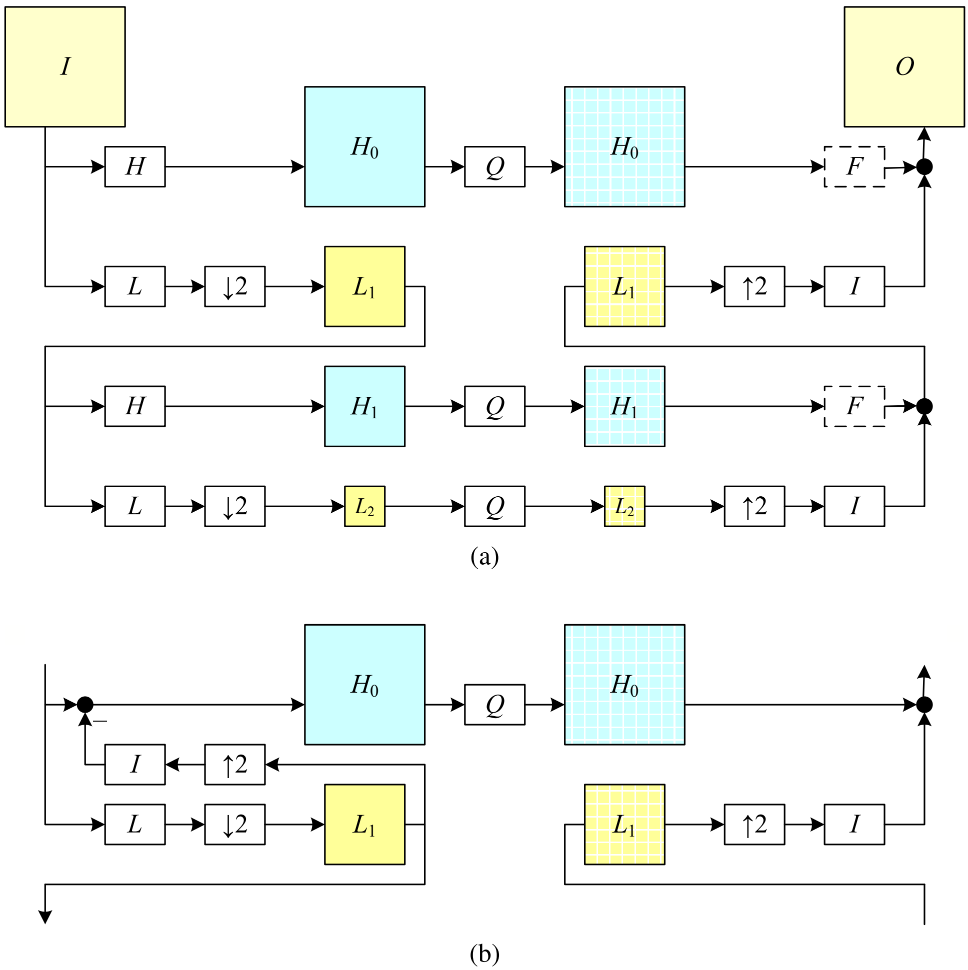


**Figure 3.34** The Laplacian pyramid: (a) The conceptual flow of images through processing stages: images are high-pass and low-pass filtered, and the low-pass filtered images are processed in the next stage of the pyramid. During reconstruction, the interpolated image and the (optionally filtered) high-pass image are added back together. The $Q$ box indicates quantization or some other pyramid processing, e.g., noise removal by *coring* (setting small wavelet values to 0). (b) The actual computation of the high-pass filter involves first interpolating the downsampled low-pass image and then subtracting it. This results in perfect reconstruction when $Q$ is the identity. The high-pass (or band-pass) images are typically called *Laplacian* images, while the low-pass images are called *Gaussian* images.

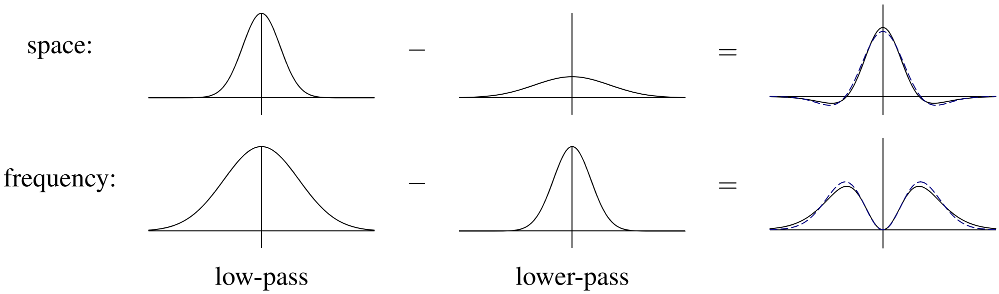


**Figure 3.35** The difference of two low-pass filters results in a band-pass filter. The dashed blue lines show the close fit to a half-octave Laplacian of Gaussian.

cent levels, the authors claim that coarse-to-fine algorithms perform better. In the image-processing community, half-octave pyramids combined with checkerboard sampling grids are known as *quincunx* sampling (Feilner, Van De Ville, and Unser 2005). In detecting multi-scale features (Section 4.1.1), it is often common to use half-octave or even quarter-octave pyramids (Lowe 2004; Triggs 2004). However, in this case, the subsampling only occurs at every octave level, i.e., the image is repeatedly blurred with wider Gaussians until a full octave of resolution change has been achieved (Figure 4.11).

### 3.5.4 Wavelets

While pyramids are used extensively in computer vision applications, some people use *wavelet* decompositions as an alternative. Wavelets are filters that localize a signal in both space and frequency (like the Gabor filter in Table 3.2) and are defined over a hierarchy of scales. Wavelets provide a smooth way to decompose a signal into frequency components without blocking and are closely related to pyramids.

Wavelets were originally developed in the applied math and signal processing communities and were introduced to the computer vision community by Mallat (1989). Strang (1989); Simoncelli and Adelson (1990b); Rioul and Vetterli (1991); Chui (1992); Meyer (1993) all provide nice introductions to the subject along with historical reviews, while Chui (1992) provides a more comprehensive review and survey of applications. Sweldens (1997) describes the more recent *lifting* approach to wavelets that we discuss shortly.

Wavelets are widely used in the computer graphics community to perform multi-resolution geometric processing (Stollnitz, DeRose, and Salesin 1996) and have also been used in computer vision for similar applications (Szeliski 1990b; Pentland 1994; Gortler and Cohen 1995; Yaou and Chang 1994; Lai and Vemuri 1997; Szeliski 2006b), as well as for multi-scale oriented filtering (Simoncelli, Freeman, Adelson *et al.* 1992) and denoising (Portilla, Strela, may become necessary to model the 3D *line* (as opposed to *direction*) corresponding to each pixel separately (Gremban, Thorpe, and Kanade 1988; Champleboux, Lavallée, Sautot *et al.* 1992; Grossberg and Nayar 2001; Sturm and Ramalingam 2004; Tardif, Sturm, Trudeau *et al.* 2009). Some of these techniques are described in more detail in Section 6.3.5, which discusses how to calibrate lens distortions.

There is one subtle issue associated with the simple radial distortion model that is often glossed over. We have introduced a non-linearity between the perspective projection and final sensor array projection steps. Therefore, we cannot, in general, post-multiply an arbitrary $3 \times 3$ matrix $\boldsymbol{K}$ with a rotation to put it into upper-triangular form and absorb this into the global rotation. However, this situation is not as bad as it may at first appear. For many applications, keeping the simplified diagonal form of (2.59) is still an adequate model. Furthermore, if we correct radial and other distortions to an accuracy where straight lines are preserved, we have essentially converted the sensor back into a linear imager and the previous decomposition still applies.

## 2.2 Photometric image formation

In modeling the image formation process, we have described how 3D geometric features in the world are projected into 2D features in an image. However, images are not composed of 2D features. Instead, they are made up of discrete color or intensity values. Where do these values come from? How do they relate to the lighting in the environment, surface properties and geometry, camera optics, and sensor properties (Figure 2.14)? In this section, we develop a set of models to describe these interactions and formulate a generative process of image formation. A more detailed treatment of these topics can be found in other textbooks on computer graphics and image synthesis (Glassner 1995; Weyrich, Lawrence, Lensch *et al.* 2008; Foley, van Dam, Feiner *et al.* 1995; Watt 1995; Cohen and Wallace 1993; Sillion and Puech 1994).

### 2.2.1 Lighting

Images cannot exist without light. To produce an image, the scene must be illuminated with one or more light sources. (Certain modalities such as fluorescent microscopy and X-ray tomography do not fit this model, but we do not deal with them in this book.) Light sources can generally be divided into point and area light sources.

A point light source originates at a single location in space (e.g., a small light bulb), potentially at infinity (e.g., the sun). (Note that for some applications such as modeling soft shadows (*penumbras*), the sun may have to be treated as an area light source.) In addition to its location, a point light source has an intensity and a color spectrum, i.e., a distribution over

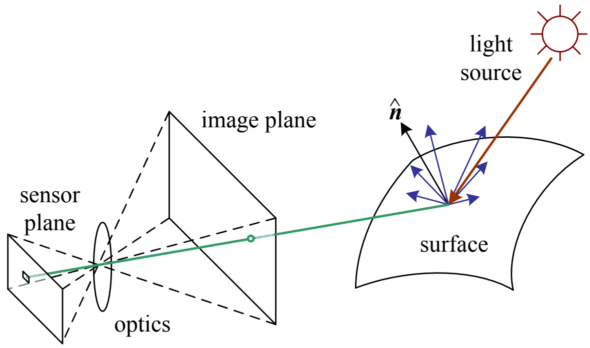


**Figure 2.14** A simplified model of photometric image formation. Light is emitted by one or more light sources and is then reflected from an object's surface. A portion of this light is directed towards the camera. This simplified model ignores multiple reflections, which often occur in real-world scenes.

wavelengths $L(\lambda)$. The intensity of a light source falls off with the square of the distance between the source and the object being lit, because the same light is being spread over a larger (spherical) area. A light source may also have a directional falloff (dependence), but we ignore this in our simplified model.

Area light sources are more complicated. A simple area light source such as a fluorescent ceiling light fixture with a diffuser can be modeled as a finite rectangular area emitting light equally in all directions (Cohen and Wallace 1993; Sillion and Puech 1994; Glassner 1995). When the distribution is strongly directional, a four-dimensional lightfield can be used instead (Ashdown 1993).

A more complex light distribution that approximates, say, the incident illumination on an object sitting in an outdoor courtyard, can often be represented using an *environment map* (Greene 1986) (originally called a *reflection map* (Blinn and Newell 1976)). This representation maps incident light directions $\hat{\boldsymbol{v}}$ to color values (or wavelengths, $\lambda$),

$$L(\hat{\boldsymbol{v}}; \lambda), \tag{2.80}$$

and is equivalent to assuming that all light sources are at infinity. Environment maps can be represented as a collection of cubical faces (Greene 1986), as a single longitude–latitude map (Blinn and Newell 1976), or as the image of a reflecting sphere (Watt 1995). A convenient way to get a rough model of a real-world environment map is to take an image of a reflective mirrored sphere and to unwrap this image onto the desired environment map (Debevec 1998). Watt (1995) gives a nice discussion of environment mapping, including the formulas needed to map directions to pixels for the three most commonly used representations.

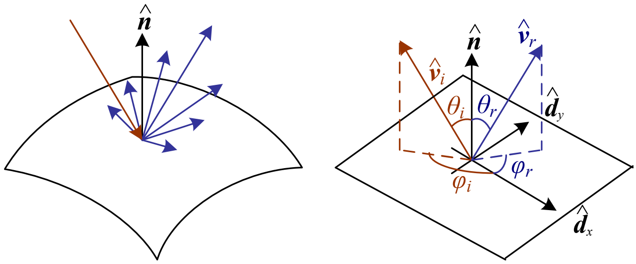


(a) (b)

**Figure 2.15** (a) Light scatters when it hits a surface. (b) The bidirectional reflectance distribution function (BRDF) $f(\theta_i, \phi_i, \theta_r, \phi_r)$ is parameterized by the angles that the incident, $\hat{\boldsymbol{v}}_i$, and reflected, $\hat{\boldsymbol{v}}_r$, light ray directions make with the local surface coordinate frame $(\hat{\boldsymbol{d}}_x, \hat{\boldsymbol{d}}_y, \hat{\boldsymbol{n}})$.

### 2.2.2 Reflectance and shading

When light hits an object's surface, it is scattered and reflected (Figure 2.15a). Many different models have been developed to describe this interaction. In this section, we first describe the most general form, the bidirectional reflectance distribution function, and then look at some more specialized models, including the diffuse, specular, and Phong shading models. We also discuss how these models can be used to compute the *global illumination* corresponding to a scene.

#### The Bidirectional Reflectance Distribution Function (BRDF)

The most general model of light scattering is the *bidirectional reflectance distribution function* (BRDF).[5] Relative to some local coordinate frame on the surface, the BRDF is a four-dimensional function that describes how much of each wavelength arriving at an *incident* direction $\hat{\boldsymbol{v}}_i$ is emitted in a *reflected* direction $\hat{\boldsymbol{v}}_r$ (Figure 2.15b). The function can be written in terms of the angles of the incident and reflected directions relative to the surface frame as

$$f_r(\theta_i, \phi_i, \theta_r, \phi_r; \lambda). \tag{2.81}$$

The BRDF is *reciprocal*, i.e., because of the physics of light transport, you can interchange the roles of $\hat{\boldsymbol{v}}_i$ and $\hat{\boldsymbol{v}}_r$ and still get the same answer (this is sometimes called *Helmholtz reciprocity*).

[5] Actually, even more general models of light transport exist, including some that model spatial variation along the surface, sub-surface scattering, and atmospheric effects—see Section 12.7.1—(Dorsey, Rushmeier, and Sillion 2007; Weyrich, Lawrence, Lensch *et al.* 2008).

Most surfaces are *isotropic*, i.e., there are no preferred directions on the surface as far as light transport is concerned. (The exceptions are *anisotropic* surfaces such as brushed (scratched) aluminum, where the reflectance depends on the light orientation relative to the direction of the scratches.) For an isotropic material, we can simplify the BRDF to

$$f_r(\theta_i, \theta_r, |\phi_r - \phi_i|; \lambda) \ \text{ or } \ f_r(\hat{\boldsymbol{v}}_i, \hat{\boldsymbol{v}}_r, \hat{\boldsymbol{n}}; \lambda), \tag{2.82}$$

since the quantities $\theta_i$, $\theta_r$ and $\phi_r - \phi_i$ can be computed from the directions $\hat{\boldsymbol{v}}_i$, $\hat{\boldsymbol{v}}_r$, and $\hat{\boldsymbol{n}}$.

To calculate the amount of light exiting a surface point $\boldsymbol{p}$ in a direction $\hat{\boldsymbol{v}}_r$ under a given lighting condition, we integrate the product of the incoming light $L_i(\hat{\boldsymbol{v}}_i; \lambda)$ with the BRDF (some authors call this step a *convolution*). Taking into account the *foreshortening* factor $\cos^+ \theta_i$, we obtain

$$L_r(\hat{\boldsymbol{v}}_r; \lambda) = \int L_i(\hat{\boldsymbol{v}}_i; \lambda) f_r(\hat{\boldsymbol{v}}_i, \hat{\boldsymbol{v}}_r, \hat{\boldsymbol{n}}; \lambda) \cos^+ \theta_i \, d\hat{\boldsymbol{v}}_i, \tag{2.83}$$

where

$$\cos^+ \theta_i = \max(0, \cos \theta_i). \tag{2.84}$$

If the light sources are discrete (a finite number of point light sources), we can replace the integral with a summation,

$$L_r(\hat{\boldsymbol{v}}_r; \lambda) = \sum_i L_i(\lambda) f_r(\hat{\boldsymbol{v}}_i, \hat{\boldsymbol{v}}_r, \hat{\boldsymbol{n}}; \lambda) \cos^+ \theta_i. \tag{2.85}$$

BRDFs for a given surface can be obtained through physical modeling (Torrance and Sparrow 1967; Cook and Torrance 1982; Glassner 1995), heuristic modeling (Phong 1975), or through empirical observation (Ward 1992; Westin, Arvo, and Torrance 1992; Dana, van Ginneken, Nayar *et al.* 1999; Dorsey, Rushmeier, and Sillion 2007; Weyrich, Lawrence, Lensch *et al.* 2008).[6] Typical BRDFs can often be split into their *diffuse* and *specular* components, as described below.

### Diffuse reflection

The diffuse component (also known as *Lambertian* or *matte* reflection) scatters light uniformly in all directions and is the phenomenon we most normally associate with *shading*, e.g., the smooth (non-shiny) variation of intensity with surface normal that is seen when observing a statue (Figure 2.16). Diffuse reflection also often imparts a strong *body color* to the light since it is caused by selective absorption and re-emission of light inside the object's material (Shafer 1985; Glassner 1995).

[6] See http://www1.cs.columbia.edu/CAVE/software/curet/ for a database of some empirically sampled BRDFs.

**Figure 2.16** This close-up of a statue shows both diffuse (smooth shading) and specular (shiny highlight) reflection, as well as darkening in the grooves and creases due to reduced light visibility and interreflections. (Photo courtesy of the Caltech Vision Lab, http://www.vision.caltech.edu/archive.html.)

While light is scattered uniformly in all directions, i.e., the BRDF is constant,

$$f_d(\hat{\boldsymbol{v}}_i, \hat{\boldsymbol{v}}_r, \hat{\boldsymbol{n}}; \lambda) = f_d(\lambda), \tag{2.86}$$

the amount of light depends on the angle between the incident light direction and the surface normal $\theta_i$. This is because the surface area exposed to a given amount of light becomes larger at oblique angles, becoming completely self-shadowed as the outgoing surface normal points away from the light (Figure 2.17a). (Think about how you orient yourself towards the sun or fireplace to get maximum warmth and how a flashlight projected obliquely against a wall is less bright than one pointing directly at it.) The *shading equation* for diffuse reflection can thus be written as

$$L_d(\hat{\boldsymbol{v}}_r; \lambda) = \sum_i L_i(\lambda) f_d(\lambda) \cos^+ \theta_i = \sum_i L_i(\lambda) f_d(\lambda) [\hat{\boldsymbol{v}}_i \cdot \hat{\boldsymbol{n}}]^+, \tag{2.87}$$

where

$$[\hat{\boldsymbol{v}}_i \cdot \hat{\boldsymbol{n}}]^+ = \max(0, \hat{\boldsymbol{v}}_i \cdot \hat{\boldsymbol{n}}). \tag{2.88}$$

### Specular reflection

The second major component of a typical BRDF is *specular* (gloss or highlight) reflection, which depends strongly on the direction of the outgoing light. Consider light reflecting off a mirrored surface (Figure 2.17b). Incident light rays are reflected in a direction that is rotated by 180° around the surface normal $\hat{\boldsymbol{n}}$. Using the same notation as in Equations (2.29–2.30),

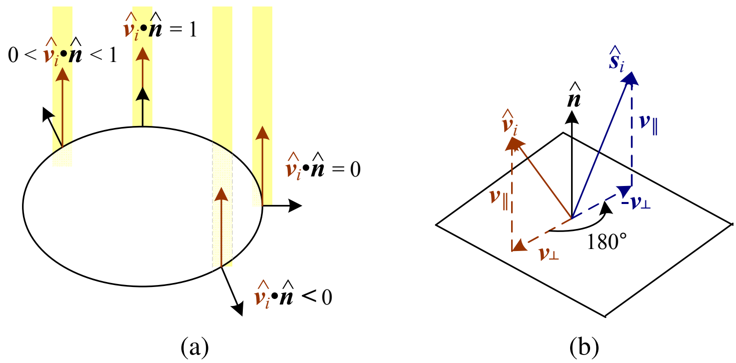


**Figure 2.17** (a) The diminution of returned light caused by *foreshortening* depends on $\hat{\boldsymbol{v}}_i \cdot \hat{\boldsymbol{n}}$, the cosine of the angle between the incident light direction $\hat{\boldsymbol{v}}_i$ and the surface normal $\hat{\boldsymbol{n}}$. (b) Mirror (specular) reflection: The incident light ray direction $\hat{\boldsymbol{v}}_i$ is reflected onto the specular direction $\hat{\boldsymbol{s}}_i$ around the surface normal $\hat{\boldsymbol{n}}$.

we can compute the *specular reflection* direction $\hat{\boldsymbol{s}}_i$ as

$$\hat{\boldsymbol{s}}_i = \boldsymbol{v}_\parallel - \boldsymbol{v}_\perp = (2\hat{\boldsymbol{n}}\hat{\boldsymbol{n}}^T - \boldsymbol{I})\boldsymbol{v}_i. \tag{2.89}$$

The amount of light reflected in a given direction $\hat{\boldsymbol{v}}_r$ thus depends on the angle $\theta_s = \cos^{-1}(\hat{\boldsymbol{v}}_r \cdot \hat{\boldsymbol{s}}_i)$ between the view direction $\hat{\boldsymbol{v}}_r$ and the specular direction $\hat{\boldsymbol{s}}_i$. For example, the Phong (1975) model uses a power of the cosine of the angle,

$$f_s(\theta_s; \lambda) = k_s(\lambda) \cos^{k_e} \theta_s, \tag{2.90}$$

while the Torrance and Sparrow (1967) micro-facet model uses a Gaussian,

$$f_s(\theta_s; \lambda) = k_s(\lambda) \exp(-c_s^2 \theta_s^2). \tag{2.91}$$

Larger exponents $k_e$ (or inverse Gaussian widths $c_s$) correspond to more specular surfaces with distinct highlights, while smaller exponents better model materials with softer gloss.

### Phong shading

Phong (1975) combined the diffuse and specular components of reflection with another term, which he called the *ambient illumination*. This term accounts for the fact that objects are generally illuminated not only by point light sources but also by a general diffuse illumination corresponding to inter-reflection (e.g., the walls in a room) or distant sources, such as the

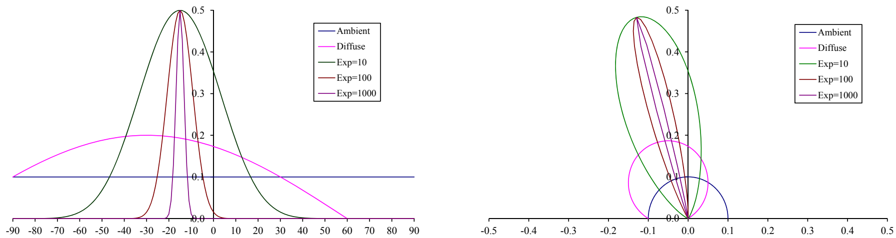


(a) (b)

**Figure 2.18** Cross-section through a Phong shading model BRDF for a fixed incident illumination direction: (a) component values as a function of angle away from surface normal; (b) polar plot. The value of the Phong exponent $k_e$ is indicated by the "Exp" labels and the light source is at an angle of 30° away from the normal.

blue sky. In the Phong model, the ambient term does not depend on surface orientation, but depends on the color of both the ambient illumination $L_a(\lambda)$ and the object $k_a(\lambda)$,

$$f_a(\lambda) = k_a(\lambda) L_a(\lambda). \tag{2.92}$$

Putting all of these terms together, we arrive at the *Phong shading* model,

$$L_r(\hat{\boldsymbol{v}}_r; \lambda) = k_a(\lambda) L_a(\lambda) + k_d(\lambda) \sum_i L_i(\lambda) [\hat{\boldsymbol{v}}_i \cdot \hat{\boldsymbol{n}}]^+ + k_s(\lambda) \sum_i L_i(\lambda) (\hat{\boldsymbol{v}}_r \cdot \hat{\boldsymbol{s}}_i)^{k_e}. \tag{2.93}$$

Figure 2.18 shows a typical set of Phong shading model components as a function of the angle away from the surface normal (in a plane containing both the lighting direction and the viewer).

Typically, the ambient and diffuse reflection color distributions $k_a(\lambda)$ and $k_d(\lambda)$ are the same, since they are both due to sub-surface scattering (body reflection) inside the surface material (Shafer 1985). The specular reflection distribution $k_s(\lambda)$ is often uniform (white), since it is caused by interface reflections that do not change the light color. (The exception to this are *metallic* materials, such as copper, as opposed to the more common *dielectric* materials, such as plastics.)

The ambient illumination $L_a(\lambda)$ often has a different color cast from the direct light sources $L_i(\lambda)$, e.g., it may be blue for a sunny outdoor scene or yellow for an interior lit with candles or incandescent lights. (The presence of ambient sky illumination in shadowed areas is what often causes shadows to appear bluer than the corresponding lit portions of a scene). Note also that the diffuse component of the Phong model (or of any shading model) depends on the angle of the *incoming* light source $\hat{\boldsymbol{v}}_i$, while the specular component depends on the relative angle between the viewer $\boldsymbol{v}_r$ and the specular reflection direction $\hat{\boldsymbol{s}}_i$ (which itself depends on the incoming light direction $\hat{\boldsymbol{v}}_i$ and the surface normal $\hat{\boldsymbol{n}}$).

The Phong shading model has been superseded in terms of physical accuracy by a number of more recently developed models in computer graphics, including the model developed by Cook and Torrance (1982) based on the original micro-facet model of Torrance and Sparrow (1967). Until recently, most computer graphics hardware implemented the Phong model but the recent advent of programmable pixel shaders makes the use of more complex models feasible.

### Di-chromatic reflection model

The Torrance and Sparrow (1967) model of reflection also forms the basis of Shafer's (1985) *di-chromatic reflection model*, which states that the apparent color of a uniform material lit from a single source depends on the sum of two terms,

$$L_r(\hat{\boldsymbol{v}}_r;\lambda) = L_i(\hat{\boldsymbol{v}}_r,\hat{\boldsymbol{v}}_i,\hat{\boldsymbol{n}};\lambda) + L_b(\hat{\boldsymbol{v}}_r,\hat{\boldsymbol{v}}_i,\hat{\boldsymbol{n}};\lambda) \tag{2.94}$$

$$= c_i(\lambda)m_i(\hat{\boldsymbol{v}}_r,\hat{\boldsymbol{v}}_i,\hat{\boldsymbol{n}}) + c_b(\lambda)m_b(\hat{\boldsymbol{v}}_r,\hat{\boldsymbol{v}}_i,\hat{\boldsymbol{n}}), \tag{2.95}$$

i.e., the radiance of the light reflected at the *interface*, $L_i$, and the radiance reflected at the *surface body*, $L_b$. Each of these, in turn, is a simple product between a relative power spectrum $c(\lambda)$, which depends only on wavelength, and a magnitude $m(\hat{\boldsymbol{v}}_r,\hat{\boldsymbol{v}}_i,\hat{\boldsymbol{n}})$, which depends only on geometry. (This model can easily be derived from a generalized version of Phong's model by assuming a single light source and no ambient illumination, and re-arranging terms.) The di-chromatic model has been successfully used in computer vision to segment specular colored objects with large variations in shading (Klinker 1993) and more recently has inspired local two-color models for applications such Bayer pattern demosaicing (Bennett, Uyttendaele, Zitnick *et al.* 2006).

### Global illumination (ray tracing and radiosity)

The simple shading model presented thus far assumes that light rays leave the light sources, bounce off surfaces visible to the camera, thereby changing in intensity or color, and arrive at the camera. In reality, light sources can be shadowed by occluders and rays can bounce multiple times around a scene while making their trip from a light source to the camera.

Two methods have traditionally been used to model such effects. If the scene is mostly specular (the classic example being scenes made of glass objects and mirrored or highly polished balls), the preferred approach is *ray tracing* or *path tracing* (Glassner 1995; Akenine-Möller and Haines 2002; Shirley 2005), which follows individual rays from the camera across multiple bounces towards the light sources (or vice versa). If the scene is composed mostly of uniform albedo simple geometry illuminators and surfaces, *radiosity* (*global illumination*) techniques are preferred (Cohen and Wallace 1993; Sillion and Puech 1994; Glassner 1995).

Combinations of the two techniques have also been developed (Wallace, Cohen, and Greenberg 1987), as well as more general *light transport* techniques for simulating effects such as the *caustics* cast by rippling water.

The basic ray tracing algorithm associates a light ray with each pixel in the camera image and finds its intersection with the nearest surface. A *primary* contribution can then be computed using the simple shading equations presented previously (e.g., Equation (2.93)) for all light sources that are visible for that surface element. (An alternative technique for computing which surfaces are illuminated by a light source is to compute a *shadow map*, or *shadow buffer*, i.e., a rendering of the scene from the light source's perspective, and then compare the depth of pixels being rendered with the map (Williams 1983; Akenine-Möller and Haines 2002).) Additional *secondary* rays can then be cast along the specular direction towards other objects in the scene, keeping track of any attenuation or color change that the specular reflection induces.

Radiosity works by associating lightness values with rectangular surface areas in the scene (including area light sources). The amount of light interchanged between any two (mutually visible) areas in the scene can be captured as a *form factor*, which depends on their relative orientation and surface reflectance properties, as well as the $1/r^2$ fall-off as light is distributed over a larger effective sphere the further away it is (Cohen and Wallace 1993; Sillion and Puech 1994; Glassner 1995). A large linear system can then be set up to solve for the final lightness of each area patch, using the light sources as the forcing function (right hand side). Once the system has been solved, the scene can be rendered from any desired point of view. Under certain circumstances, it is possible to recover the global illumination in a scene from photographs using computer vision techniques (Yu, Debevec, Malik *et al.* 1999).

The basic radiosity algorithm does not take into account certain *near field* effects, such as the darkening inside corners and scratches, or the limited ambient illumination caused by partial shadowing from other surfaces. Such effects have been exploited in a number of computer vision algorithms (Nayar, Ikeuchi, and Kanade 1991; Langer and Zucker 1994).

While all of these global illumination effects can have a strong effect on the appearance of a scene, and hence its 3D interpretation, they are not covered in more detail in this book. (But see Section 12.7.1 for a discussion of recovering BRDFs from real scenes and objects.)

### 2.2.3 Optics

Once the light from a scene reaches the camera, it must still pass through the lens before reaching the sensor (analog film or digital silicon). For many applications, it suffices to treat the lens as an ideal pinhole that simply projects all rays through a common center of projection (Figures 2.8 and 2.9).

However, if we want to deal with issues such as focus, exposure, vignetting, and aber-

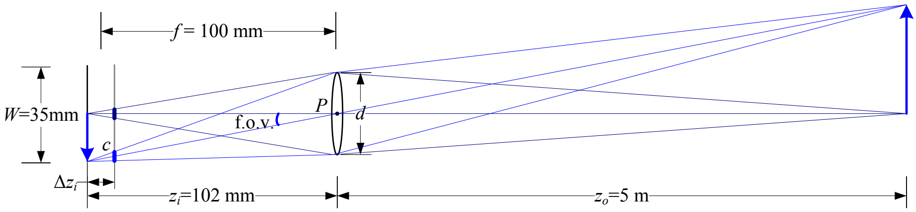


**Figure 2.19** A thin lens of focal length $f$ focuses the light from a plane a distance $z_o$ in front of the lens at a distance $z_i$ behind the lens, where $\frac{1}{z_o} + \frac{1}{z_i} = \frac{1}{f}$. If the focal plane (vertical gray line next to $c$) is moved forward, the images are no longer in focus and the *circle of confusion* $c$ (small thick line segments) depends on the distance of the image plane motion $\Delta z_i$ relative to the lens aperture diameter $d$. The field of view (f.o.v.) depends on the ratio between the sensor width $W$ and the focal length $f$ (or, more precisely, the focusing distance $z_i$, which is usually quite close to $f$).

ration, we need to develop a more sophisticated model, which is where the study of *optics* comes in (Möller 1988; Hecht 2001; Ray 2002).

Figure 2.19 shows a diagram of the most basic lens model, i.e., the *thin lens* composed of a single piece of glass with very low, equal curvature on both sides. According to the *lens law* (which can be derived using simple geometric arguments on light ray refraction), the relationship between the distance to an object $z_o$ and the distance behind the lens at which a focused image is formed $z_i$ can be expressed as

$$\frac{1}{z_o} + \frac{1}{z_i} = \frac{1}{f}, \tag{2.96}$$

where $f$ is called the *focal length* of the lens. If we let $z_o \rightarrow \infty$, i.e., we adjust the lens (move the image plane) so that objects at infinity are in focus, we get $z_i = f$, which is why we can think of a lens of focal length $f$ as being equivalent (to a first approximation) to a pinhole a distance $f$ from the focal plane (Figure 2.10), whose field of view is given by (2.60).

If the focal plane is moved away from its proper in-focus setting of $z_i$ (e.g., by twisting the focus ring on the lens), objects at $z_o$ are no longer in focus, as shown by the gray plane in Figure 2.19. The amount of mis-focus is measured by the *circle of confusion* $c$ (shown as short thick blue line segments on the gray plane).[7] The equation for the circle of confusion can be derived using similar triangles; it depends on the distance of travel in the focal plane $\Delta z_i$ relative to the original focus distance $z_i$ and the diameter of the aperture $d$ (see Exercise 2.4).

[7] If the aperture is not completely circular, e.g., if it is caused by a hexagonal diaphragm, it is sometimes possible to see this effect in the actual blur function (Levin, Fergus, Durand *et al.* 2007; Joshi, Szeliski, and Kriegman 2008) or in the "glints" that are seen when shooting into the sun.

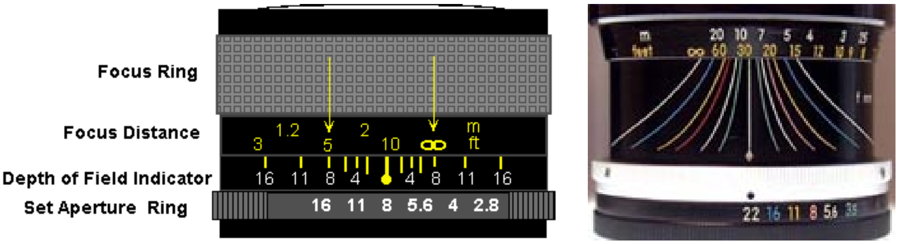


(a) (b)

**Figure 2.20** Regular and zoom lens depth of field indicators.

The allowable depth variation in the scene that limits the circle of confusion to an acceptable number is commonly called the *depth of field* and is a function of both the focus distance and the aperture, as shown diagrammatically by many lens markings (Figure 2.20). Since this depth of field depends on the aperture diameter $d$, we also have to know how this varies with the commonly displayed *f-number*, which is usually denoted as $f/\#$ or $N$ and is defined as

$$f/\# = N = \frac{f}{d}, \tag{2.97}$$

where the focal length $f$ and the aperture diameter $d$ are measured in the same unit (say, millimeters).

The usual way to write the f-number is to replace the $\#$ in $f/\#$ with the actual number, i.e., $f/1.4, f/2, f/2.8, \ldots, f/22$. (Alternatively, we can say $N = 1.4$, etc.) An easy way to interpret these numbers is to notice that dividing the focal length by the f-number gives us the diameter $d$, so these are just formulas for the aperture diameter.[8]

Notice that the usual progression for f-numbers is in *full stops*, which are multiples of $\sqrt{2}$, since this corresponds to doubling the area of the entrance pupil each time a smaller f-number is selected. (This doubling is also called changing the exposure by one *exposure value* or EV. It has the same effect on the amount of light reaching the sensor as doubling the exposure duration, e.g., from $^1/_{125}$ to $^1/_{250}$, see Exercise 2.5.)

Now that you know how to convert between f-numbers and aperture diameters, you can construct your own plots for the depth of field as a function of focal length $f$, circle of confusion $c$, and focus distance $z_o$, as explained in Exercise 2.4 and see how well these match what you observe on actual lenses, such as those shown in Figure 2.20.

Of course, real lenses are not infinitely thin and therefore suffer from geometric aberrations, unless compound elements are used to correct for them. The classic five *Seidel aberrations*, which arise when using *third-order optics*, include spherical aberration, coma, astigmatism, curvature of field, and distortion (Möller 1988; Hecht 2001; Ray 2002).

[8] This also explains why, with zoom lenses, the f-number varies with the current zoom (focal length) setting.

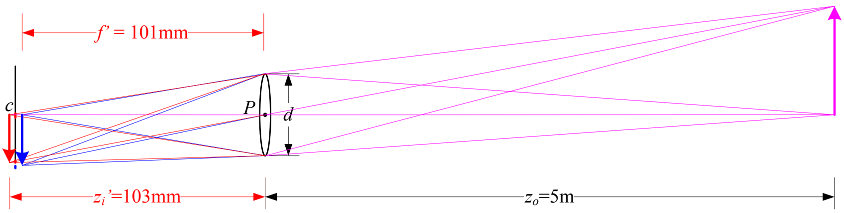


**Figure 2.21** In a lens subject to *chromatic aberration*, light at different wavelengths (e.g., the red and blur arrows) is focused with a different focal length $f'$ and hence a different depth $z_i'$, resulting in both a geometric (in-plane) displacement and a loss of focus.

### Chromatic aberration

Because the index of refraction for glass varies slightly as a function of wavelength, simple lenses suffer from *chromatic aberration*, which is the tendency for light of different colors to focus at slightly different distances (and hence also with slightly different magnification factors), as shown in Figure 2.21. The wavelength-dependent magnification factor, i.e., the *transverse chromatic aberration*, can be modeled as a per-color radial distortion (Section 2.1.6) and, hence, calibrated using the techniques described in Section 6.3.5. The wavelength-dependent blur caused by *longitudinal chromatic aberration* can be calibrated using techniques described in Section 10.1.4. Unfortunately, the blur induced by longitudinal aberration can be harder to undo, as higher frequencies can get strongly attenuated and hence hard to recover.

In order to reduce chromatic and other kinds of aberrations, most photographic lenses today are *compound lenses* made of different glass elements (with different coatings). Such lenses can no longer be modeled as having a single *nodal point* $P$ through which all of the rays must pass (when approximating the lens with a pinhole model). Instead, these lenses have both a *front nodal point*, through which the rays enter the lens, and a *rear nodal point*, through which they leave on their way to the sensor. In practice, only the location of the front nodal point is of interest when performing careful camera calibration, e.g., when determining the point around which to rotate to capture a parallax-free panorama (see Section 9.1.3).

Not all lenses, however, can be modeled as having a single nodal point. In particular, very wide-angle lenses such as fisheye lenses (Section 2.1.6) and certain *catadioptric* imaging systems consisting of lenses and curved mirrors (Baker and Nayar 1999) do not have a single point through which all of the acquired light rays pass. In such cases, it is preferable to explicitly construct a mapping function (look-up table) between pixel coordinates and 3D rays in space (Gremban, Thorpe, and Kanade 1988; Champleboux, Lavallée, Sautot *et al.*

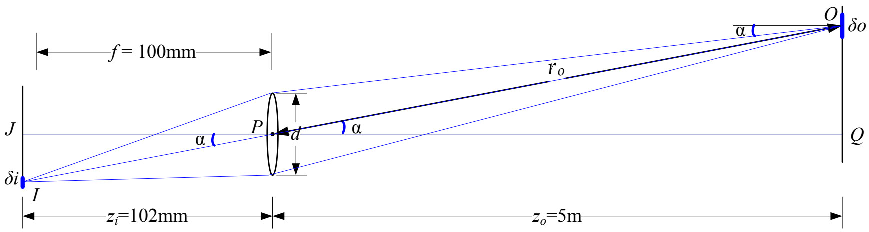


**Figure 2.22** The amount of light hitting a pixel of surface area $\delta i$ depends on the square of the ratio of the aperture diameter $d$ to the focal length $f$, as well as the fourth power of the off-axis angle $\alpha$ cosine, $\cos^4 \alpha$.

1992; Grossberg and Nayar 2001; Sturm and Ramalingam 2004; Tardif, Sturm, Trudeau *et al.* 2009), as mentioned in Section 2.1.6.

### Vignetting

Another property of real-world lenses is *vignetting*, which is the tendency for the brightness of the image to fall off towards the edge of the image.

Two kinds of phenomena usually contribute to this effect (Ray 2002). The first is called *natural vignetting* and is due to the foreshortening in the object surface, projected pixel, and lens aperture, as shown in Figure 2.22. Consider the light leaving the object surface patch of size $\delta o$ located at an *off-axis angle* $\alpha$. Because this patch is foreshortened with respect to the camera lens, the amount of light reaching the lens is reduced by a factor $\cos \alpha$. The amount of light reaching the lens is also subject to the usual $1/r^2$ fall-off; in this case, the distance $r_o = z_o / \cos \alpha$. The actual area of the aperture through which the light passes is foreshortened by an additional factor $\cos \alpha$, i.e., the aperture as seen from point $O$ is an ellipse of dimensions $d \times d \cos \alpha$. Putting all of these factors together, we see that the amount of light leaving $O$ and passing through the aperture on its way to the image pixel located at $I$ is proportional to

$$\frac{\delta o \cos \alpha}{r_o^2} \pi \left( \frac{d}{2} \right)^2 \cos \alpha = \delta o \frac{\pi}{4} \frac{d^2}{z_o^2} \cos^4 \alpha. \tag{2.98}$$

Since triangles $\Delta OPQ$ and $\Delta IPJ$ are similar, the projected areas of of the object surface $\delta o$ and image pixel $\delta i$ are in the same (squared) ratio as $z_o : z_i$,

$$\frac{\delta o}{\delta i} = \frac{z_o^2}{z_i^2}. \tag{2.99}$$

Putting these together, we obtain the final relationship between the amount of light reaching pixel $i$ and the aperture diameter $d$, the focusing distance $z_i \approx f$, and the off-axis angle $\alpha$,

$$\delta o \frac{\pi}{4} \frac{d^2}{z_o^2} \cos^4 \alpha = \delta i \frac{\pi}{4} \frac{d^2}{z_i^2} \cos^4 \alpha \approx \delta i \frac{\pi}{4} \left(\frac{d}{f}\right)^2 \cos^4 \alpha, \tag{2.100}$$

which is called the *fundamental radiometric relation* between the scene radiance $L$ and the light (irradiance) $E$ reaching the pixel sensor,

$$E = L \frac{\pi}{4} \left(\frac{d}{f}\right)^2 \cos^4 \alpha, \tag{2.101}$$

(Horn 1986; Nalwa 1993; Hecht 2001; Ray 2002). Notice in this equation how the amount of light depends on the pixel surface area (which is why the smaller sensors in point-and-shoot cameras are so much noisier than digital single lens reflex (SLR) cameras), the inverse square of the f-stop $N = f/d$ (2.97), and the fourth power of the $\cos^4 \alpha$ off-axis fall-off, which is the natural vignetting term.

The other major kind of vignetting, called *mechanical vignetting*, is caused by the internal occlusion of rays near the periphery of lens elements in a compound lens, and cannot easily be described mathematically without performing a full ray-tracing of the actual lens design.[9] However, unlike natural vignetting, mechanical vignetting can be decreased by reducing the camera aperture (increasing the f-number). It can also be calibrated (along with natural vignetting) using special devices such as integrating spheres, uniformly illuminated targets, or camera rotation, as discussed in Section 10.1.3.

## 2.3 The digital camera

After starting from one or more light sources, reflecting off one or more surfaces in the world, and passing through the camera's optics (lenses), light finally reaches the imaging sensor. How are the photons arriving at this sensor converted into the digital (R, G, B) values that we observe when we look at a digital image? In this section, we develop a simple model that accounts for the most important effects such as exposure (gain and shutter speed), non-linear mappings, sampling and aliasing, and noise. Figure 2.23, which is based on camera models developed by Healey and Kondepudy (1994); Tsin, Ramesh, and Kanade (2001); Liu, Szeliski, Kang *et al.* (2008), shows a simple version of the processing stages that occur in modern digital cameras. Chakrabarti, Scharstein, and Zickler (2009) developed a sophisticated 24-parameter model that is an even better match to the processing performed in today's cameras.

[9] There are some empirical models that work well in practice (Kang and Weiss 2000; Zheng, Lin, and Kang 2006).